Direct Frequency Modulation in AlGaAs Semiconductor Lasers

SOICHI KOBAYASHI, MEMBER, IEEE, YOSHIHISA YAMAMOTO, MEMBER, IEEE, MINORU ITO, AND TATSUYA KIMURA, SENIOR MEMBER, IEEE

Abstract—Direct frequency modulation characteristics in three different AlGaAs lasers—a channeled-substrate planar (CSP) laser, a buried-heterostructure (BH) laser, and a transverse-junction-stripe (TJS) laser—are studied theoretically and experimentally. Experimental FM responses are measured by using the Fabry–Perot interferometer and birefringent optical filters in the 0–5.2 GHz modulation frequency region. Experimental FM response dependences on modulation frequency, dc bias level, and stripe structure are successfully explained by the theoretical analyses considering both the carrier density modulation effect and the temperature change effect. FM response in the low modulation frequency region from 0 to 10 MHz, gradually decreasing with the modulation frequency, stems from the thermal effect. FM response in the high modulation frequency region from 10 MHz to 5.2 GHz is caused by the carrier effect. A flat FM response of several hundred MHz per 1 mA is observed in the CSP and TJS lasers, but a V-shaped FM response is obtained in the BH laser. Resonance peak due to relaxation oscillation and cutoff characteristics are observed in several gigahertz regions. Weak lateral mode confinement, strong vertical mode confinement, carrier injection outside the effective core region, and p-side down mounts are effective ways to achieve a flat and efficient FM response with a small spurious intensity modulation.

I. INTRODUCTION

OPTICAL FIBER transmission systems developed so far have employed optical energy transmission with intensity modulation and direct detection. Repeater spacing expansion and transmission capacity improvement are expected in the coherent optical fiber transmission system, utilizing an angle modulation of coherent laser wave, a single polarization mode fiber, and an optical heterodyne (or homodyne) detection [1], [2]. An initial trial of a coherent optical modulation–demodulation experiment has been successfully demonstrated using direct frequency modulation of an AlGaAs laser transmitter and optical heterodyne detection with an independent AlGaAs local oscillator [3], [4].

The direct frequency modulation capability of a semiconductor laser through an injection current modulation [5], [6] is promising for the applications to the coherent transmission system, since an FM transmitter and a tunable local oscillator can be realized with a conventional semiconductor laser. A large frequency shift by a small modulation current without serious unintended intensity modulation is desired for the above applications.

This paper describes experimental and theoretical studies on the optical frequency modulation characteristics of AlGaAs semiconductor lasers. Three different AlGaAs semiconductor lasers—a channeled-substrate planar (CSP) laser, a buried-heterostructure (BH) laser, and a transverse-junction-stripe (TJS) laser—were tested. Preliminary experiments on modulation frequency characteristics have been reported [7]. The experimental frequency modulation characteristics are compared with the theoretical treatments considering both temperature and carrier density modulation effects. The FM efficiency is discussed in terms of modulation frequency, dc bias current, and diode structure together with the laser structure optimization for an FM modulation.

II. MEASUREMENT SYSTEM AND PROCEDURE

A. Experimental Setup

A diagram of the experimental setup is shown in Fig. 1. Double heterostructure AlGaAs semiconductor lasers with three different structures were tested. The three structures were 1) A CSP laser [8] with threshold current $I_{th, C} = 69$ mA, and single longitudinal mode wavelength at $\lambda_C = 840$ nm. The laser chip is mounted as that p-side electrode is in contact with a submount (p-side down). 2) A BH laser [9] mounted p-side up with threshold current $I_{th, B} = 36$ mA, and single frequency operation at the wavelength $\lambda_B = 820$ nm. 3) A TJS geometry laser [10] mounted p-side up with threshold current $I_{th, T} = 39$ mA, and emitting wavelength $\lambda_T = 840$ nm in a single frequency. A dc bias current above threshold and sinusoidal modulation current in the frequency range of 200 Hz–5.2 GHz has been applied to these lasers.

Modulation spectra are observed by two methods depending on the optical frequency excursion. The scanning Fabry–Perot interferometer has a free spectral range varied between 1.5 GHz and 10 GHz and a finesse larger than 40. For the modulation frequency range of 200 Hz–10 MHz, a temperature compensated birefringent optical filter [11] is used.

Two 4.25-cm-long calcite crystals and two 1.1-cm-long LiTaO$_3$ crystals are combined in tandem. The free spectral range of the filter is 19.3 GHz. The spurious intensity modulation depth is simultaneously monitored by using a germanium avalanche photodiode (APD) whose frequency characteristics are calibrated over 10 MHz–2 GHz by means of shot noise induced by irradiating with GaAs LED light. An optical isolator with 25 dB isolation loss [12] is used at the laser output to avoid undesired feedback from the measuring system.
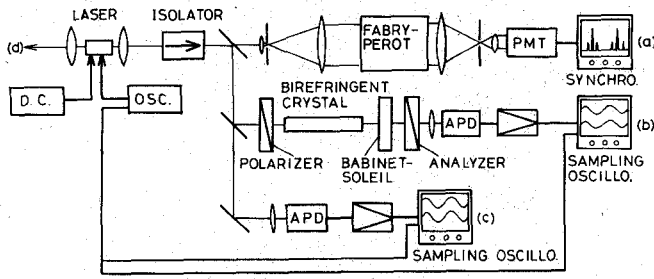
Fig. 1. Experimental setup for frequency deviation measurement. (a) Power spectra measurement by Fabry–Perot interferometer. (b) FM–AM conversion by birefringent filter. (c) Intensity modulation measurement. (d) Longitudinal mode observation.

B. Experimental Procedure

The frequency-modulated optical wave is represented by

$$E = E_0 \exp \left[j \{ 2\pi f_0 t + \beta \sin (2\pi f_m t) \} \right] \qquad (1)$$

$$\beta = \Delta F / f_m \qquad (2)$$

where f_0 is center frequency, ΔF is the maximum frequency deviation, f_m is modulation frequency, and β is the frequency modulation index.

Several methods were used in evaluating the optical frequency deviation in the present experiment, depending on the modulation frequency. Typical optical frequency spectra for the CSP laser observed by the Fabry–Perot interferometer are shown in Fig. 2. When the modulation frequency is higher than 40 MHz, the scanning Fabry–Perot interferometer output gives the optical field spectra as shown in Fig. 2(a). These particular spectra are obtained by a CSP laser for 150 MHz modulation frequency at a bias current 1.4 times the threshold $I_{th,C}$. Applied sinusoidal modulation currents are varied from 0 to 4 mA_{0-p} corresponding to Fig. 2(a)–(h). The free spectral range of the scanning Fabry–Perot interferometer is 1.5 GHz. The optical field spectrum of the frequency-modulated wave in (1) can be expanded in terms of Bessel functions $J_l(\beta)$ of the first kind

$$E = J_0(\beta) E_0 \sin (2\pi f_0 t) + J_1(\beta) E_0 \sin \{ 2\pi (f_0 + f_m) t \}$$
$$- J_1(\beta) E_0 \sin \{ 2\pi (f_0 - f_m) t \} + \cdots + J_l(\beta) E_0$$
$$\cdot \sin \{ 2\pi (f_0 + l f_m) t \} + (-1)^l J_l(\beta) E_0$$
$$\cdot \sin \{ 2\pi (f_0 - l f_m) t \}. \qquad (3)$$

Each observed sideband intensity corresponds to the square of the coefficient of corresponding terms in (3). Frequency modulation index β can be obtained from the ratio of the carrier and the first sideband intensity.

When the modulation frequency is between 10 kHz and 30 MHz at which a large frequency deviation is expected with a low modulation drive current, an FM spectrum with a large frequency deviation is used to measure β as shown in Fig. 2(i). For a frequency modulation index larger than 20, twice the maximum frequency deviation $2\Delta F$ is directly observed from the separation between two sideband peaks. The particular spectrum shown in Fig. 2(i) is obtained at 100 kHz modulation frequency, 0.43 mA_{0-p} modulation current, and maxi-
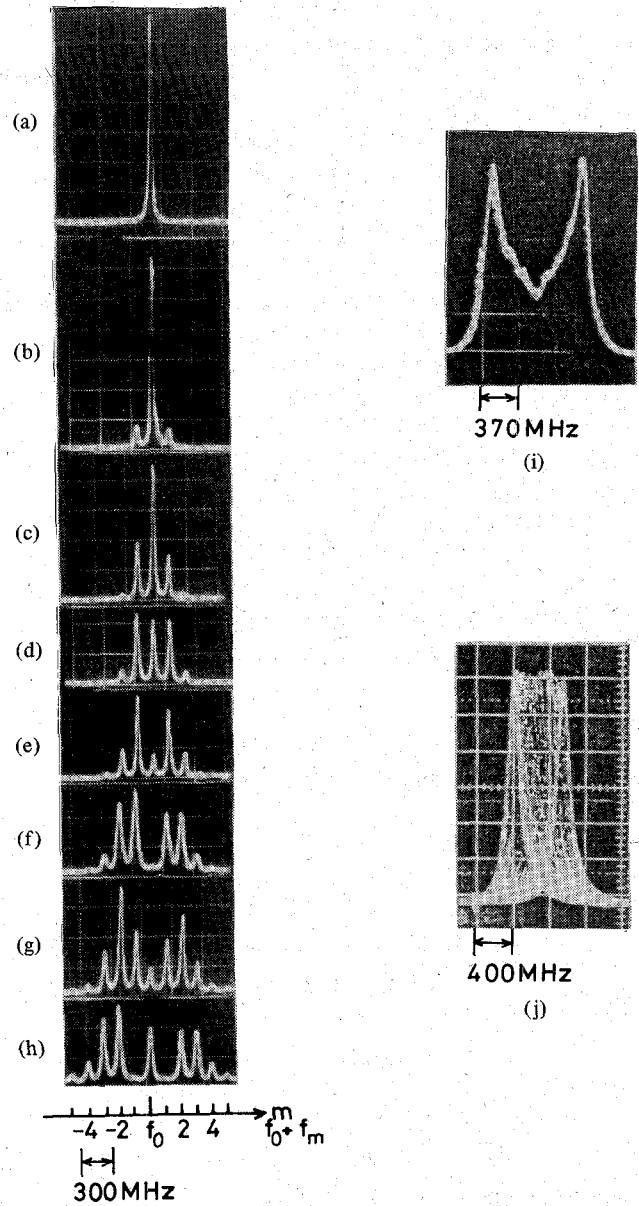

370 MHz
(i)

400 MHz
(j)

Fig. 2. Power spectra for a directly modulated CSP laser measured by Fabry–Perot interferometer. (a)–(h) f_m = 150 MHz, I = 1.4 × $I_{th,C}$, $I_{th,C}$ = 69 mA. ΔI_{0-p} = (a) 0 mA, (b) 0.76 mA, (c) 1.4 mA, (d) 1.84 mA, (e) 2.24 mA, (f) 2.88 mA, (g) 3.44 mA, (h) 4 mA. FSR is 1.5 GHz. (i) f_m = 100 kHz, I = 1.5 × $I_{th,C}$, ΔI_{0-p} = 0.43 mA, and FSR = 1.9 GHz. (j) f_m = 400 Hz, I = 1.5 × $I_{th,C}$, ΔI_{0-p} = 0.11 mA, and FSR = 1.9 GHz.

mum frequency deviation ΔF = 442 MHz_{0-p}. The free spectral range of the scanning Fabry–Perot interferometer is 1.9 GHz.

At modulation frequency lower than 1 kHz, the scanning Fabry–Perot interferometer output shows the instantaneous frequency shift on an oscilloscope display, as shown in Fig. 2(j). This spectrum corresponds to 340 MHz_{0-p} maximum frequency deviation at 0.11 mA_{0-p} modulation current and 400 Hz modulation frequency. The Fabry–Perot scanning frequency is 885 Hz.

At the intermediate modulation frequency range between 200 Hz and 50 kHz, FM–AM conversion by means of a birefringent optical filter is useful. The high frequency limit of

this method is imposed by the spurious AM component contained in the directly frequency-modulated output.

When the center frequency f_0 of the sinusoidally modulated laser is shifted from the balance frequency of the discriminator, optical output through the birefringent filter is changed as shown in Fig. 3(a)-(e). The modulation frequency is 20 kHz and modulation current is 0.6 mA_{0-p}. Half the free spectral range, 9.6 GHz, corresponds to the frequency shift f_0 between (a) and (e) in Fig. 3. After confirming the linear relation between the frequency shift and output intensity at the balance frequency of the discriminator as shown in Fig. 3(c), the maximum frequency deviation was measured as $\Delta F = 1.32$ GHz_{0-p}.

The optical frequency deviation for dc current was measured by the scanning Fabry-Perot interferometer. The deviation for the CSP laser is 3.1 GHz/mA and is independent of the bias current. Obtained results by using the above measuring method for the total modulation frequency range between 200 kHz and 5.2 GHz are shown in Fig. 4. The ordinate shows the amount of frequency deviation per unit modulation current. A CSP laser at a bias current 1.5 times the threshold is used under the condition that the spurious AM modulation index is less than 5 percent.

III. EXPERIMENTAL RESULT

A. FM and AM Modulation Indices of Direct Frequency Modulation

The optical sideband spectra of a directly current-modulated semiconductor laser are asymmetrical, as shown in Fig. 2(a)-(h). The upper sideband amplitude is smaller than that of the lower sideband. This is caused by an AM modulation superimposed on the FM modulation. A simultaneous FM and AM modulated optical wave is represented as follows:

$$E = E_0 \{1 + M \cos (2\pi f_m t)\}$$
$$\cdot \exp [j\{2\pi f_0 t + \beta \sin (2\pi f_m t)\}] \quad (4)$$

$$f = f_0 + \Delta F \cos (2\pi f_m t) \quad (5)$$

where f is the instantaneous frequency and M is the amplitude modulation index. By expanding (4), carrier and first sideband amplitudes are represented as follows:

Carrier:

$$J_0 E_0 \exp \{j(2\pi f_0 t)\}. \quad (6)$$

Upper first sideband:

$$[J_1(\beta) + (M/2) \{J_2(\beta) + J_0(\beta)\}] E_0$$
$$\cdot \exp \{j2\pi(f_0 + f_m) t\}. \quad (7)$$

Lower first sideband:

$$[-J_1(\beta) + (M/2) \{J_2(\beta) + J_0(\beta)\}] E_0$$
$$\cdot \exp \{j2\pi(f_0 - f_m)\}t. \quad (8)$$

These equations show that the first upper sideband amplitude is larger than that of the lower sideband when the FM and AM are in phase. When the two modulations are out of phase, the upper sideband amplitude is smaller than that of the lower sideband, which is in agreement with the obtained experimental results shown in Fig. 2(a)-(h) (see Appendix I). These
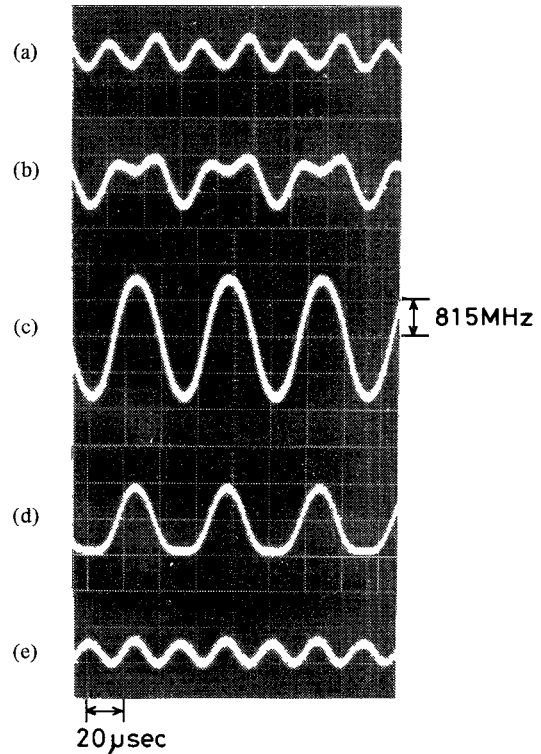

Fig. 3. Optical output converted from FM to AM signal emitted from directly modulated CSP laser by a birefringent filter. The birefringent filter is composed of two 4.25-cm-long calcite crystals and two 1.1-cm-long $LiTaO_3$ crystals. FSR is 19.3 GHz. $f_m = 20$ kHz, $\Delta F_{0-p} = 1.32$ GHz, and $\Delta I = 0.94$ mA. Horizontal scale means time and vertical scale means frequency. Peak-to-peak wave amplitude shows twice the frequency deviation $2\Delta F$.
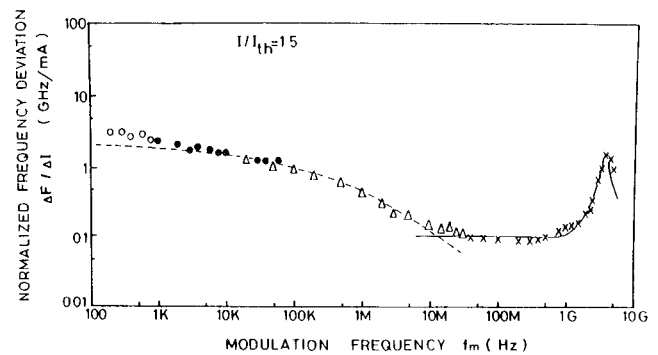

Fig. 4. Frequency deviation per unit sinusoidal modulation current amplitude in a CSP laser. Measurement method indicated by (a)-(c) corresponds to (a)-(h) ~ (j) of those in Fig. 2. See text for detail procedure. $I = 1.5 \times I_{th}$. Experimental: (a) ×××️ Fabry-Perot; (b) △△△ Fabry-Perot; (c) ∘∘∘ Fabry-Perot; ●●● birefringent filter. Theoretical: ---- thermal effect; —— carrier effect.

equations also show that the FM modulation index can be obtained from the average value of the upper and lower sideband amplitudes, while the AM modulation depth can be obtained from their difference.

Fig. 5 shows the normalized amplitude for carrier and various sidebands as a function of modulation current. Marks corresponding to sidebands were experimentally obtained by averaging the upper and lower sideband amplitudes to remove the AM component. Solid curves show the theoretical Bessel function values. Fig. 6 shows maximum frequency deviation ΔF in the CSP laser as a function of modulation current ΔI
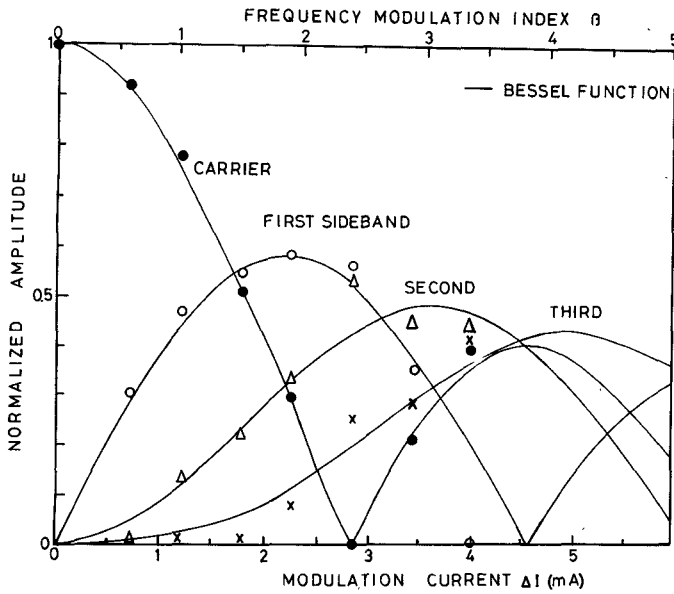
Fig. 5. Normalized amplitude for various order of sidebands observed in the power spectra of Fig. 2 (a)-(h) versus modulation current and frequency modulation index. •: carrier, o: first sideband, Δ: second sideband, and X: third sideband. Solid lines show theoretical value of Bessel function values of the first kind.

Fig. 7. Normalized frequency deviation for a CSP laser versus modulation frequency. o: $I = 1.1 \times I_{th,C}$, •: $I = 1.2 \times I_{th,C}$, Δ: $I = 1.3 \times I_{th,C}$, X: $I = 1.4 \times I_{th,C}$, and ▼: $I = 1.5 \times I_{th,C}$. Solid lines show calculated values considering lateral carrier diffusion.

The spurious AM modulation index is kept less than 5 percent. Frequency characteristics of the laser drive circuit and receiver circuit are calibrated by using intensity modulation of the laser at a bias current 1.35 times the threshold. Solid line curves are theoretical values obtained by the rate equation analysis considering photon and carrier distribution in the active layer and lateral carrier diffusion effect, which will be discussed in Section IV. The frequency deviation at a unit modulation current is constant in the modulation frequency range from 50 MHz to 1 GHz. The deviation depends on the dc bias current in this frequency range. It shows resonant characteristics at above 1 GHz. As the bias current increases, the resonant frequency increases and the peak value decreases.

In the low modulation frequency region less than 50 MHz, the frequency deviation behavior is different from that in the high frequency region. A large frequency deviation is caused by temperature rise in the active layer which is caused by the modulation current. The deviation in this frequency range becomes independent of the bias current.

Comparison of the frequency modulation and intensity modulation characteristics is of interest. Fig. 8 shows the normalized modulation efficiency of intensity modulation as a function of modulation frequency in the same CSP laser. Various symbols show experimental results at various bias currents from 1.04 to 1.14 times the threshold in the modulation frequency region from 10 MHz to 2 GHz. The frequency characteristics of driver and receiver circuits are calibrated as previously described. The IM frequency characteristics at a frequency less than 500 MHz is independent of the bias current. The resonant frequency and peak values are in good agreement with the theoretical values calculated by the first-order rate equation [13] indicated by solid line curves. The resonant frequencies for FM and AM obtained from Figs. 7 and 8 are plotted in Fig. 9. Open and closed circles show FM and IM resonant frequencies, respectively. The solid line represents the theoretical value calculated by the rate equation, as shown in Fig. 7. Theoretical details will be discussed in Section IV. The IM resonant frequency has been measured
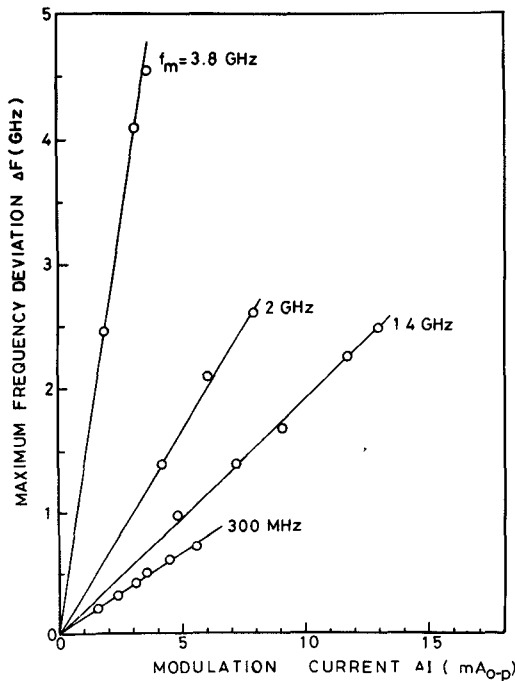

Fig. 6. Maximum frequency deviation for a CSP laser versus modulation current.

at a bias current 1.4 times the threshold $I_{th,C}$. The frequency deviation increases linearly with the modulation current. These gradients increase with the increase in modulation frequency.

B. Bias Current Dependence of Frequency Deviation

Frequency deviation in the CSP laser normalized by modulation current is shown in Fig. 7 as a function of modulation frequency. Various marks show experimental results at various bias currents from 1.1 to 1.5 times the threshold $I_{th,C}$.
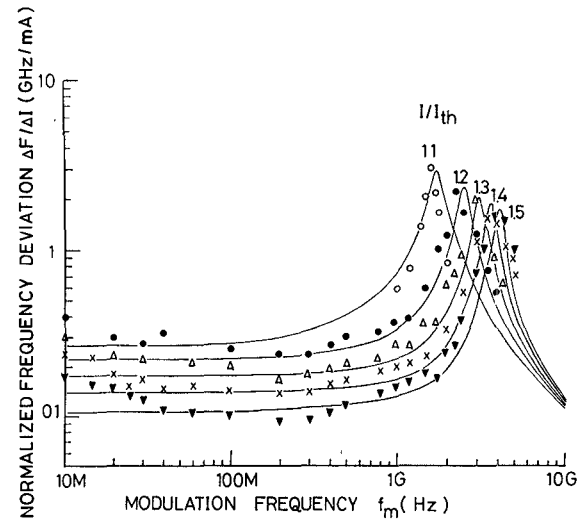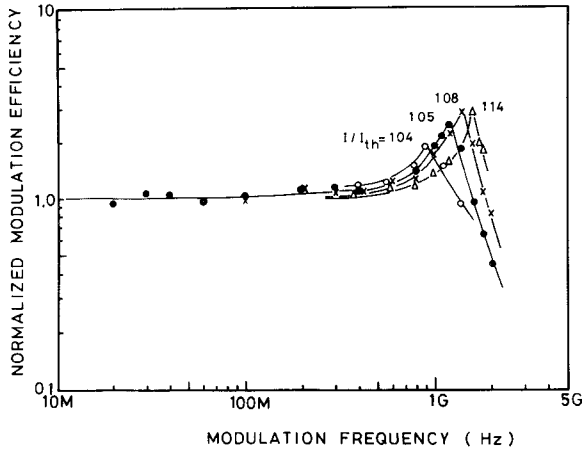
Fig. 8. Normalized modulation efficiency for intensity modulation for a CSP laser versus modulation frequency. o: $I = 1.04 \times I_{th,C}$, •: $I = 1.05 \times I_{th,C}$, X: $I = 1.08 \times I_{th,C}$, and △: $I = 1.14 \times I_{th,C}$.
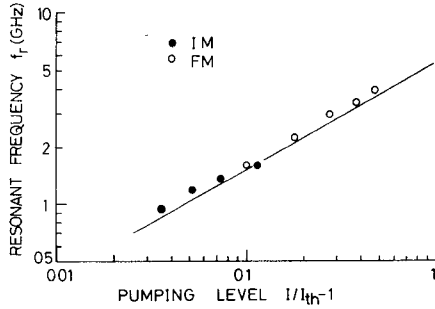

Fig. 9. Resonant frequency of FM and IM modulation versus dc drive current. o: FM modulation and •: IM modulation. Solid line shows the calculated results as shown in Fig. 7.

up to $1.14 \times I_{th,C}$, while the FM resonant frequency has been measured up to the modulation frequency limit decided by the free spectral range (FSR) of the Fabry–Perot interferometer. Experimental results show good agreement with the theoretical values.

C. Frequency Deviation Characteristics for TJS, CSP, and BH Lasers

Fig. 10 shows the frequency deviations per unit modulation current as a function of modulation frequency for the TJS, CSP, and BH lasers in the frequency region between 200 Hz and 5.2 GHz. Bias levels are 1.17, 1.17, and 1.25 times each threshold for the TJS, CSP, and BH lasers, respectively. Three kinds of lines in the figure show theoretical values for three kinds of lasers obtained by the theoretical analyses considering carrier density modulation effect and temperature modulation effect. A theoretical discussion as well as the laser structure effect will be discussed and presented in detail in Section IV.

At above 1 GHz, each laser shows similar resonant phenomena. The frequency deviation values for the TJS and BH lasers at resonant frequencies are the same, while the value for the CSP laser is smaller than those for TJS and BH lasers. There is a shallow dip of the frequency deviation value in the TJS laser at 1 GHz. The TJS and CSP lasers show a flat response in the frequency range between 10 MHz and 1 GHz, while V-shaped characteristics are observed in the BH laser. The frequency deviation values decrease in the order of the TJS, CSP, and BH lasers except for those values at the resonant peak. In the frequency region below 10 MHz, frequency characteristics show

monotonically decreasing characteristics with the modulation frequency. The frequency deviation values for the TJS and BH lasers are nearly the same, while those for the CSP laser are lower than those for the other two. Low frequency characteristics are governed by thermal effect. The difference in the frequency deviations is caused by different thermal impedances. The CSP laser is mounted p-side down and has a low thermal impedance, while the TJS and BH lasers have high impedance values due to their p-side up mounts. A theoretical explanation of the modulation characteristics will be discussed in the next section by taking the carrier and temperature induced index change into account.

IV. THEORETICAL ANALYSIS

Carrier density and temperature, in a semiconductor laser active layer, are changed by the injection current modulation. Both are responsible for the refractive-index modulation, that is, the resonant axial mode frequency modulation in a semiconductor laser. This section presents a theoretical discussion on the frequency modulation due to a carrier density modulation effect and a temperature change effect.

A. Carrier Density Modulation Effect

The normalized oscillation frequency deviation due to carrier density modulation is

$$\Delta F_C/f_0 = (C_{BB} + C_{FC})(\Gamma_y/\bar{n})\int \Delta N_e(x)|\epsilon(x)|^2 \, dx \qquad (9)$$

where f_0 is an optical oscillation frequency of about 3.57×10^{14} Hz, Γ_y is the mode confinement factor along the vertical direction, $\bar{n}$ is the average refractive-index of the active layer, $\Delta N_e(x)$ is the distribution of carrier density modulation along the lateral direction, and $\epsilon(x)$ is the normalized optical lasing field which satisfies $\int_{-\infty}^{\infty} |\epsilon(x)|^2 \, dx = 1$. The function $\epsilon(x)^2$ is calculated for a specific diode structure with the values of effective core width W_{eff} and effective refractive index difference Δ_{eff}. The values of W_{eff} and Δ_{eff} for CSP, TJS, and BH lasers tested here are obtained from the manufacturer's data [8]-[10] and summarized in Table I.

Coefficients C_{FC} and C_{BB}, relating the carrier density change to the refractive-index change, represent the free carrier plasma disperson effect [14] and the anomalous dispersion effect due to band-to-band transition [15]. The value of $C_{FC} = -1.8 \times 10^{-21}$ cm^{-3} is obtained by

$$C_{FC} = -e^2/(2m'\omega^2\epsilon_0\bar{n}) \qquad (10)$$

where m' is the effective mass of an electron and $\bar{n}$ is the refractive index. The value of $C_{BB} = -2.6 \times 10^{-21}$ cm^{-3} is assumed here for the transition between the exponential bandtail in the conduction band and the parabolic valence band. The sum of C_{BB} and C_{FC} is estimated to be -4.4×10^{-21} cm^{-3}, which agrees well with the experimental value [16].

The distribution of carrier density modulation $\Delta N_e(x)$ along the lateral direction is calculated by the Statz–de Mars type rate equation with lateral carrier and optical field distributions

$$dN_e(x)/dt = J(x)/ed - N_e(x)/\tau_s + (L_D^2/\tau_s)(d^2N_e(x)/dx^2)$$
$$- \alpha\Gamma_y[N_e(x) - N_e^0] S(x) \qquad (11)$$

$$dS(x)/dt = \alpha\Gamma_y[N_e(x) - N_e^0] S(x) + \beta_s\zeta(N_e(x)/\tau_s)$$
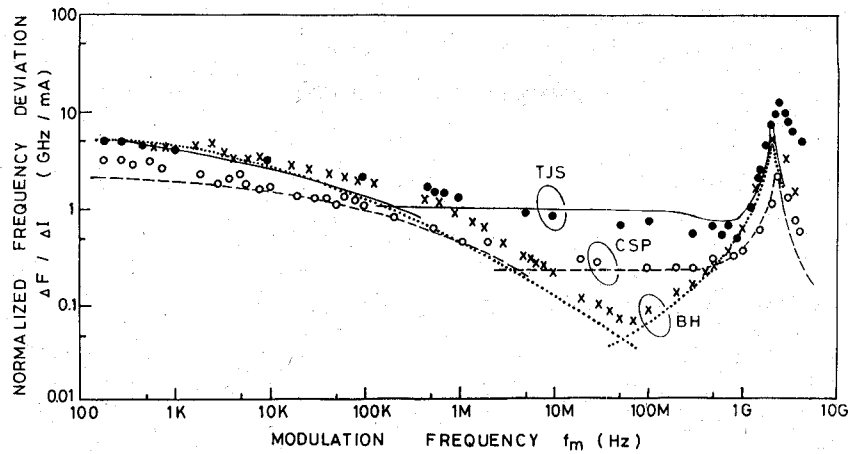$$- S(x)/\tau_p. \qquad (12)$$

Fig. 10. Normalized frequency deviation for TJS, CSP, and BH lasers versus modulation frequency. Experimental: ●: TJS laser, $I = 1.17 \times I_{th,T}$, bias current is $I_{th,T} = 39$ mA. ○: CSP laser, $I = 1.17 \times I_{th,C}$, $I_{th,C} = 69$ mA. ✕: BH laser, $I = 1.25 \times I_{th,B}$, $I_{th,B} = 36$ mA. Theoretical: ———: TJS laser, ———: CSP laser, and ······: BH laser.

TABLE I
DIRECT FREQUENCY MODULATION CHARACTERISTICS AND NUMERICAL PARAMETERS FOR CSP, TJS, AND BH LASERS

	CSP	TJS	BH
Δf_s / ΔI (MHz/mA)	250	750	85
Δf_s at 10 % IM (I/I_{th} = 1.2, f_m = 50 MHz)	300	500	77
Threshold current	69 mA	39 mA	36 mA
Effective core width W_{eff}	6 μm	2 μm	2.5 μm
Refractive-index difference Δ_{eff}	1×10⁻³	2×10⁻³ (p-p) 5~10×10⁻³ (p-n)	1.1×10⁻¹
Stripe width A	$A > W_{eff}$	$A > W_{eff}$	$A = W_{eff}$
Mode confinement factor Γ_y	0.13	0.52	0.17

Layers	h_i (μm)	K_i (W/μm) ×10⁻⁴	κ_i (μm²/s) ×10⁸	h_i (μm)	K_i (W/μm) ×10⁻⁴	κ_i (μm²/s) ×10⁸	h_i (μm)	K_i (W/μm) ×10⁻⁴	κ_i (μm²/s) ×10⁸
1st	1.6	0.1	0.05	3.0	0.1	0.05	1.0	0.1	0.05
2nd	0.4	0.1	0.05	1.5	0.1	0.05	1.5	0.1	0.05
3rd	0.8	0.4	0.27	60	0.45	0.27	50	0.45	0.27
4th	50	0.45	0.27	1.5	0.4	0.27	1.5	0.1	0.05
5th	0.8	3.2	1.0	1.0	3.18	1.26	1.0	3.18	1.26
6th	0.3	3.2	1.0	0.5	3.18	1.26	0.5	3.18	1.26
7th	0.2	0.87	0.6	2.0	0.87	0.5	2.0	0.87	0.5

Here $J(x)/ed$ is the pumping rate, τ_s is the spontaneous lifetime, L_D is the carrier diffusion length, τ_p is the photon lifetime, and β_s is the fraction of spontaneous emission coupled into a lasing mode given by

$$\beta_s = \Gamma_y \lambda^4 / 4\pi^2 n^3 \Delta \lambda_s V_I \qquad (13)$$

where $\Delta \lambda_s$ is the spontaneous emission linewidth and $V_I (= A \times d \times L)$ is the active layer volume. The photon density $S(x)$ of a lasing mode is equal to $S_0 |\epsilon(x)|^2$, where $S_0 = \int_{-\infty}^{\infty} S(x)\, dx$.

The coupling parameter ζ between carrier and optical field is defined as

$$\zeta = A \int_{-\infty}^{\infty} N_e(x)|\epsilon(x)|^2\, dx / \int_{-\infty}^{\infty} N_e(x)\, dx \qquad (14)$$

where A is the stripe width, which is the same as the effective core width W_{eff} for the BH laser but is broader than W_{eff} for the CSP and TJS lasers. Notice that the value of ζ approaches unity for the structure in which an optical field is well confined within the stripe width and that ζ is less than unity for the vice versa.

The numerical evaluation of $\Delta N_e(x)$ is carried out by the Runge–Kutta calculation of (11) and (12) [13]. Initial values of $N_e(x)$ and $S(x)$ at $t = 0$ are obtained by the steady-state rate equations in the integral form

$$(\zeta/A) \int_{-\infty}^{\infty} J(x)/ed\, dx - N/\tau_s - \alpha\Gamma_y \zeta [N - N_e^0] S = 0 \qquad (15)$$

$$\alpha\Gamma_y [N - N_e^0] S - S/\tau_p + \beta_s(N_e/\tau_s) = 0 \qquad (16)$$

where

$$S \equiv \int_{-\infty}^{\infty} S(x)\, dx/A \qquad (17)$$

$$N \equiv \int_{-\infty}^{\infty} N_e(x)|\epsilon(x)|^2\, dx. \qquad (18)$$

The threshold current is obtained from the following equation:

$$J_{th} = (ed/\tau_s)(N_e^0 + 1/\alpha\Gamma_y\tau_p)/\zeta_{(J=J_{th})}. \qquad (19)$$

The active layer is divided into 201 equally spaced regions, where carrier and photon density values are assumed to be constant. For a given $J(x)$, steady-state values for S, N, and $N_e(x)$ are obtained from (15) and (16). The Runge–Kutta calculation is performed using these initial solutions at time interval $\Delta t = 0.1$ ps.

The distribution of carrier density modulation $\Delta N_e(x)$ is approximately calculated by the perturbation analysis of (11)

and (12). Carrier and photon densities are approximately expressed as follows:

$$N_e(x) = \begin{cases} N_0 - N_1 \cos(2\pi x/W_{\text{eff}}) - N_2 \cos(\pi x/W_{\text{eff}}) \\ \qquad\qquad\qquad\qquad\qquad |x| \leqslant W_{\text{eff}}/2 \\ N_0 + N_1 - N_2 \cos(\pi x/W_{\text{eff}}) \\ \qquad\qquad\qquad\qquad\qquad |x| \geqslant W_{\text{eff}}/2 \end{cases} \quad (20)$$

$$S(x) = \begin{cases} 2S_0 \left[\cos^2(\pi x/W_{\text{eff}}) + \eta \cos^2(\pi x/2 W_{\text{eff}})\right] \\ \qquad\qquad\qquad\qquad\qquad |x| \leqslant W_{\text{eff}}/2 \\ 2\eta S_0 \cos^2(\pi x/2 W_{\text{eff}}) \qquad |x| \geqslant W_{\text{eff}}/2 \end{cases} \quad (21)$$

where η is the normalized optical field intensity at the effective core-cladding boundary. Second-order perturbation terms N_2 and η, which are neglected in the previous perturbation theory developed for intensity modulation analysis [17], [18], play an important role in frequency modulation characteristics, as described later. By substituting (20) and (21) into (11) and (12), we obtain the following set of rate equations:

$$dS_0/dt = -S_0/\tau_p + (\beta_s \zeta/\tau_s)[N_0 - N_1/2(1 + \eta)$$
$$\qquad - \eta N_2/2(1 + \eta)] + \alpha\Gamma_y S_0 [N_0 - N_1/2(1 + \eta)$$
$$\qquad - \eta N_2/2(1 + \eta) - N_e^0] \qquad (22)$$

$$dN_0/dt = P - N_0/\tau_s - \alpha\Gamma_y S_0 [N_0 - N_1/2(1 + \eta)$$
$$\qquad - \eta N_2/2(1 + \eta) - N_e^0] \qquad (23)$$

$$dN_1/dt = -N_1/\tau_s - (L_D^2/\tau_s)(2\pi/W_{\text{eff}})^2 N_1$$
$$\qquad + \alpha\Gamma_y S_0 [N_0/(1 + \eta) - N_1 - \eta N_2/2(1 + \eta)$$
$$\qquad - N_e^0/(1 + \eta)] \qquad (24)$$

$$dN_2/dt = -N_2/\tau_2 - (L_D^2/\tau_s)(\pi/W_{\text{eff}})^2 N_2$$
$$\qquad + \alpha\Gamma_y S_0 [\eta(N_0 - N_e^0)/(1 + \eta) - \eta N_1/2(1 + \eta)$$
$$\qquad - (3 + 2\eta)N_2/2(1 + \eta)] . \qquad (25)$$

The steady-state solutions of S_0, N_0, N_1, and N_2 are obtained by the following transcendental equation:

$$J/ed - \overline{N}_{\text{eff}}/\tau_s + (L_D^2/2\pi)(2\pi/W_{\text{eff}})^2 \overline{N}_1$$
$$\qquad - [\alpha\Gamma_y \overline{S}_0/(1 + \eta)] [(3/2 + \eta) \overline{N}_{\text{eff}}$$
$$\qquad - \overline{N}_1/4 - 3\eta \overline{N}_2/4 - (3/2 + \eta) N_e^0 = 0 \qquad (26)$$

where

$$\overline{N}_{\text{eff}} = \overline{N}_0 - \overline{N}_1/2. \qquad (27)$$

When a small-signal modulation current at angular frequency ω is superimposed on a dc bias current $J = \overline{J} + J^m e^{j\omega t}$, the solution of (22)–(25) is assumed as the following small-signal perturbation

$$S_0 = \overline{S}_0 + S^m e^{j\omega t}$$

$$N_{\text{eff}} = \overline{N}_{\text{eff}} + N_{\text{eff}}^m e^{j\omega t}$$

$$N_1 = \overline{N}_1 + N_1^m e^{j\omega t}$$

and

$$N_2 = \overline{N}_2 + N_2^m e^{j\omega t}.$$

Thus, we obtain a set of simultaneous equations for S^m, N_{eff}^m, N_1^m, and N_2^m for a given J^m and ω

$$\begin{bmatrix} A_{ij} \end{bmatrix} \begin{bmatrix} S^m \\ N_{\text{eff}}^m \\ N_1^m \\ N_2^m \end{bmatrix} = \begin{bmatrix} 0 \\ J^m/ed \\ 0 \\ 0 \end{bmatrix} \qquad (28)$$

where elements A_{ij} are summarized in Appendix II. The distribution of carrier density modulation $\Delta N_e(x)$ is given by

$$\Delta N_e(x) = \begin{cases} (N_{\text{eff}}^m + N_1^m/2) - N_1^m \cos(2\pi x/W_{\text{eff}}) \\ \qquad - N_2^m \cos(\pi x/W_{\text{eff}}) \qquad |x| \leqslant W_{\text{eff}} \\ (N_{\text{eff}}^m + 3N_1^m/2) - N_2^m \cos(\pi x/W_{\text{eff}}) \\ \qquad\qquad\qquad\qquad\qquad |x| \geqslant W_{\text{eff}}. \end{cases} \quad (29)$$

Normalized frequency deviations $(\Delta F_c/f_0)/(J^m/J_{\text{th}})$ for a CSP laser calculated by the numerical Runge–Kutta analysis and the perturbation theory are shown in Fig. 11 as a function of modulation frequency. The present perturbation theory indicated by a dashed line in Fig. 11(b) is in reasonable agreement with the exact analysis shown by the solid line (a). The conventional first-order theory neglecting N_2 and η indicated by a dashed and dotted line (c), however, differs from the exact theory at low modulation frequency. A similar discrepancy is observed in the simple rate equation analysis assuming uniform carrier and optical field distribution along the lateral direction, which is shown by dotted line (d).

The distribution of carrier density modulation $\Delta N_e(x)$ at various modulation frequency values calculated by the exact theory is shown in Fig. 12. At modulation frequency of 3.2 GHz, carrier density modulation is enhanced in the central portion of the stripe because of the relaxation oscillation between carrier and photon densities. Therefore, frequency modulation at around this resonant modulation frequency mainly stems from $\Delta N_e(x)$ within the effective core region. Consequently, the first-order perturbation theory neglecting the effect of ΔN_e outside the effective core region is a good approximation in this modulation frequency region.

At modulation frequency lower than 3 GHz, on the other hand, carrier density modulation within the effective core region is suppressed, since the quasi-Fermi level (carrier density) is clamped by the gain saturation effect. Frequency modulation at low modulation frequency mainly stems from $\Delta N_e(x)$ outside the effective core region, where a lasing optical field is too weak to clamp the quasi-Fermi level. The first-order perturbation theory cannot account for $\Delta N_e(x)$ outside the effective core region, which is the reason for the large discrepancy between the exact analysis and the first-order perturbation theory. On the other hand, the present perturbation theory including $\Delta N_e(x)$ outside the effective core region has sufficient accuracy in the low modulation frequency range.

The experimental results on frequency modulation characteristics for CSP, TJS, and BH lasers at 10 MHz–5.2 GHz modulation frequency range are successfully explained by the present perturbation theory, as shown in Fig. 13. Numerical values for W_{eff}, Δ_{eff}, d, Γ_y, and stripe width A are determined from the manufacturer's data [8]–[10] and are summarized in Table I.
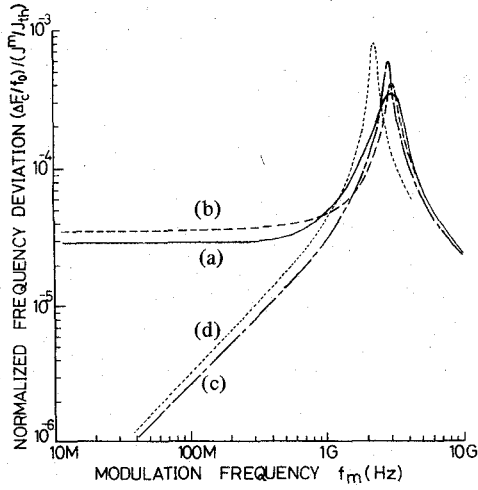
Fig. 11. Normalized frequency deviation $(\Delta F_c/f_0)/(J^m/J_{th})$ calculated for a CSP laser versus modulation frequency. (a) numerical Runge–Kutta calculation, (b) present perturbation theory, (c) conventional 1st order perturbation theory, (d) uniform carrier and optical field model. $I/I_{th} = 1.3, L_D = 3\ \mu m$.
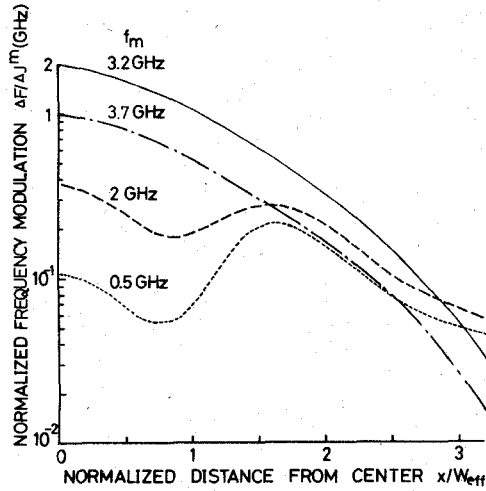

Fig. 12. Distribution of normalized carrier density modulation $\Delta N_e(x)$ at various modulation frequency values for a CSP laser at $I/I_{th}, C = 1.3$.
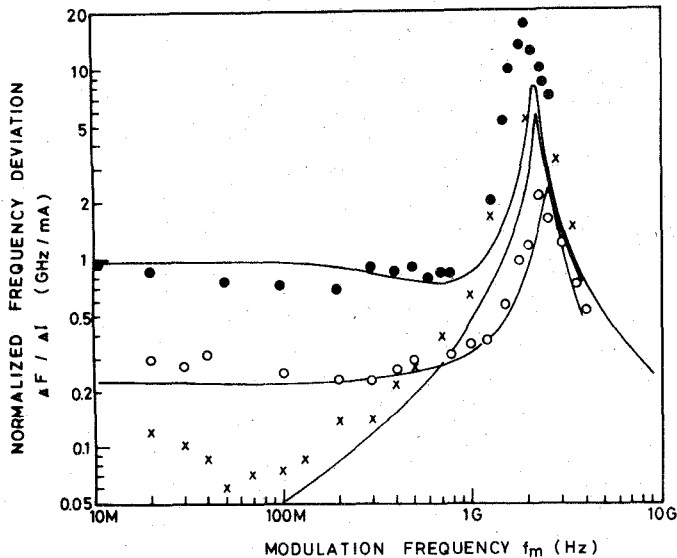

Fig. 13. Normalized frequency deviations $(\Delta F/\Delta I)$ for CSP, TJS, and BH lasers versus modulation frequency. $I/I_{th} = 1.17$ (for CSP and TJS lasers), 1.25 (for BH laser).

CSP and TJS lasers have flat FM responses at a modulation frequency range from 10 MHz to 1 GHz, but a BH laser exhibits a gradual decrease in FM response at low modulation frequency. In the BH laser, carrier and lasing optical field are well confined within the effective core region, which is responsible for the strong clamp of the quasi-Fermi level and the decrease in FM response.

In TJS and CSP lasers, the carrier spreads outside the effective core region and the lasing optical field is not so well confined within the effective core region due to their small refractive-index differences, which are favorable for flat FM responses in a low modulation frequency range. Figs. 14 and 15 show normalized frequency deviation versus modulation frequency as functions of refractive-index difference and effective core width, respectively. Flat FM response is enhanced with decreasing the lasing optical field confinement along the lateral direction. FM response for the TJS laser is larger than that for the CSP laser because of its larger vertical mode confinement factor Γ_y, smaller threshold current, and narrower effective core width.

Experimental dc bias level dependences for FM characteristics shown in Fig. 7 are successfully explained by the present perturbation theory as well as the exact numerical analysis. Normalized frequency deviation $\Delta F_c/\Delta I$ (GHz/mA) versus dc bias level $I/I_{th} - 1$ is shown in Fig. 16 for various modulation frequencies. A flat FM response between 10 MHz and 200 MHz modulation frequency is decreased with increasing dc bias current. This is because an increase in lasing optical field intensity serves to clamp the quasi-Fermi level tightly and reduce $\Delta N_e(x)$. The steeper decrease in FM response at a modulation frequency higher than 500 MHz stems from the resonant enhancement in FM response due to relaxation oscillation. The relaxation oscillation resonant frequency increases and peak FM response decreases with increasing dc bias current as shown in Fig. 16, which are the same characteristics as in the intensity modulation performance.

B. Temperature Modulation Effect

The normalized oscillation frequency deviation due to temperature modulation in an active layer is

$$\Delta F_t/f_0 = -(\alpha_L + \alpha_n)\,\Delta T_{eff}$$

$$\Delta T_{eff} = \int \Delta T_a(x)|\epsilon(x)|^2\,dx \tag{30}$$

where $\alpha_L = (1/L)\,dL/dT = 0.6 \times 10^{-5}$ (deg^{-1}) is a linear thermal expansion coefficient of GaAs, $\alpha_n = (1/n)\,dn/dT = 0.99 \times 10^{-4}$ (deg^{-1}) is a thermal refractive-index coefficient of GaAs, and ΔT_a is a distribution of temperature modulation in an active layer.

Temperature modulation $\Delta T_a(x)$ is calculated by the Fourier and Laplace transform method for the time-dependent thermal equation [19]. The structural model of a laser diode used for thermal analysis is shown in Fig. 17. Thickness h_i, thermal conductivity K_i, and thermal diffusivity κ_i in each layer are assumed to be constant for the small modulation in temperature. It is also assumed that heat is generated uniformly within stripe width A and cavity length L.

Two-dimensional heat flow in the chip and the three-dimensional heat flow in the submount, then, will be treated, including heat radiation effect from a top layer to the ambient
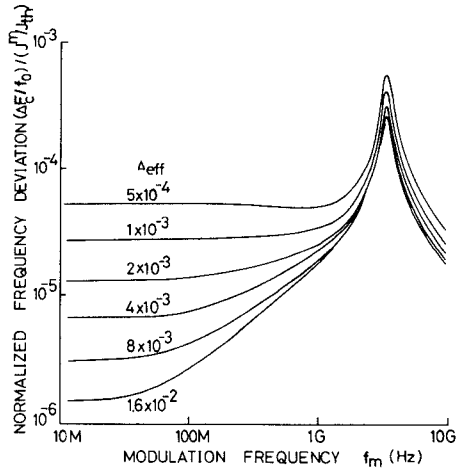
Fig. 14. Normalized frequency deviation $(\Delta F_c/f_0)/(J^m/J_{th})$ versus modulation frequency f_m as a function of refractive index difference Δ_{eff}. $I/I_{th} = 1.4$, $W_{eff} = 6~\mu m$, $L_D = 3~\mu m$, and $\Gamma_y = 0.26$.
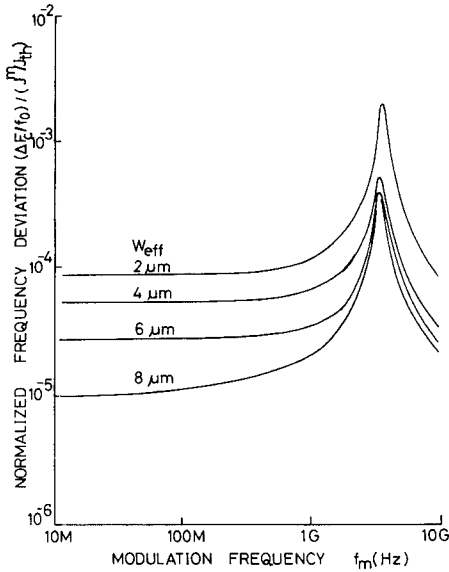

Fig. 15. Normalized frequency deviation $(\Delta F_c/f_0)/(J^m/J_{th})$ versus modulation frequency f_m as a function of effective core width W_{eff}. $I/I_{th} = 1.14$, $\Delta_{eff} = 1 \times 10^3$, $L_D = 3~\mu m$, and $\Gamma_y = 0.26$.

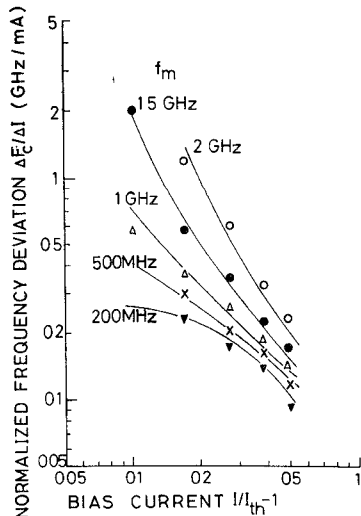Fig. 16. Normalized frequency deviation $\Delta F_c/\Delta I$ versus dc bias level. ▼: $f_m = 200$ MHz, ×: $f_m = 500$ MHz, △: $f_m = 1$ GHz, ●: $f_m = 1.5$ GHz, and ○: $f_m = 2$ GHz. Solid line curves show calculated values.
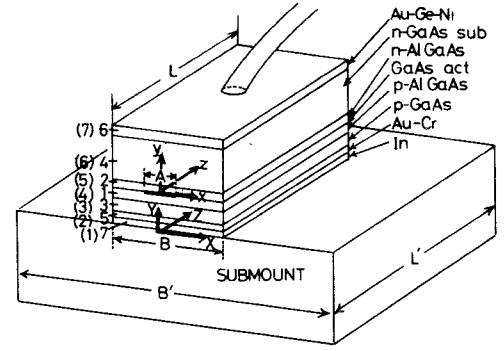

Fig. 17. Laser diode structural model used for thermal analysis.

atmosphere as well as the dominant heat transfer to a heat sink. The thermal equation in each layer i is given by

$$\partial T_i/\partial t = \kappa_i \nabla^2 T_i + W_i/C \tag{31}$$

where C is heat capacity per unit volume and W_i is heat generation power. Temperature modulation $\Delta T_a(x)$ is separately obtained for that due to the heat conduction in a diode chip itself and that due to the heat transfer in a submount.

First, temperature modulation is derived due to the heat conduction in a diode chip itself. The time-dependent heat generation function $W_{act}(W/cm^2)$ in an active layer is given by

$$W_{act} = V_D [J - \eta_L(J - J_{th}) - \eta_{sp} J_{th} - W_{sp}] \tag{32}$$

where V_D is junction voltage, J is a time varying drive current density, η_L is external quantum efficiency above a threshold current, η_{sp} is that below a threshold current, and W_{sp} is spontaneous emission power absorbed in GaAs substrate and cap layer. Here, junction voltage V_D is assumed to be independent of dc bias current because the quasi-Fermi level is fully clamped in the central portion of the stripe where lasing optical field intensity is sufficiently high.

The Laplace transform of the temperature modulation in the ith layer, due to the heat generation in an active layer, is given by

$$\hat{T}_i(x, y) = \sum_n \hat{B}_{i,n} [\cosh (\hat{\beta}_{i,n} y)$$
$$- \hat{e}_{i,n} \sinh (\hat{\beta}_{i,n} y)] \cos (k_n x) \tag{33}$$

where

$$\hat{\beta}_{i,n}^2 = p/\kappa_i^2 + k_n^2$$

$$k_n = 2\pi n/B$$

where B is a diode chip width and n is an integer. p is the Laplace operator and the sign $\wedge$ denotes a Laplacian. Coefficients $\hat{B}_{i,n}$ and $\hat{e}_{i,n}$ are determined by solving equations for temperature and heat flow continuity at the layer boundaries. They are expressed as closed form functions of h_i, $\hat{\beta}_{i,n}$, κ_i, and $\hat{W}_{act}$, and are summarized in [19].

A time-dependent heat generation function $W_r(W/cm^2)$ in an ohmic resistance is given by

$$W_r = J^2 r \tag{34}$$

where r is the total ohmic resistance in a diode chip.

The ohmic heat power is mainly generated in the p-AlGaAs cladding layer for GaAs lasers with good ohmic contacts [20]. Therefore, the temperature modulation due to the

ohmic heat generation can be calculated in the same procedure using (33), after dividing the p-AlGaAs layer into two layers and renumbering layers so that the heat generation surface is bounded by layers 1 and 2. The real time temperature modulation is evaluated by the numerical inverse Laplace transform of (33).

Next, temperature modulation will be derived due to the heat conduction in a submount. The new coordinate system (X, Y, Z) is shown in Fig. 17. Each layer is renumbered as shown in the parenthesis in Fig. 17. The Laplace transform of temperature variation in the submount is expressed by

$$T_s(X, Y, Z) = \sum_{m,l} \hat{B}_{ml} \{\cosh (\hat{\beta}_{ml} Y)$$

$$- \hat{e}_{ml} \sinh (\hat{\beta}_{ml} Y)\} \cos (k_n X) \cos (k_l Z)$$

where

$$\hat{\beta}_{ml}^2 = p/\kappa_9 + k_m^2 + k_l^2$$

$$k_n = 2n\pi/B'$$

$$k_l = l\pi/L'.$$

κ_9 is the thermal diffusivity of the submount. B' and L' are the width and the length of the submount, respectively. The coefficients $\hat{B}_{ml}^2$ and $\hat{e}_{ml}$ are summarized in [19]. The Laplace transform of temperature modulation in the ith layer due to the heat conduction in a submount is given by

$$\hat{T}_i(X) = \hat{B}_{i,o} + \sum \hat{B}_{i,n} \cos (k_n X) \tag{35}$$

where coefficients $\hat{B}_{i,o}$ and $\hat{B}_{i,n}$ are summarized in [19]. The total temperature modulation is given by the simple sum of the temperature modulations due to each heat source and due to each thermal conduction because of the linearity in thermal equation (31).

The experimental results on frequency modulation characteristics at low modulation frequency for CSP, TJS, and BH lasers are successfully explained by the present thermal analysis, as shown in Fig. 10. Numerical parameters used for thermal analysis are determined from microscopic observation of the etched facet and manufacturer's data. They are summarized in Table I. TJS and BH lasers have higher FM response than the CSP laser because of their p-side up mounting; or, in other words, because of the large distance between an active layer and a submount surface. Experimental FM response at low modulation frequency is almost independent of a dc bias current, as shown in Fig. 18. This is because the ohmic heat generation which depends on dc bias current is less than one-fourth of the heat generation in an active layer, which is almost independent of a dc bias current due to clamping the junction voltage to V_{th} above the threshold.

Theoretical normalized frequency deviation over the 0–5.2 GHz modulation frequency range including both carrier density modulation and temperature modulation effects are shown in Fig. 10. From the comparison between experimental and theoretical results, it is concluded that frequency modulation at low modulation frequency stems from the temperature modulation effect and that frequency modulation at high modulation frequency stems from the carrier density modulation effect.
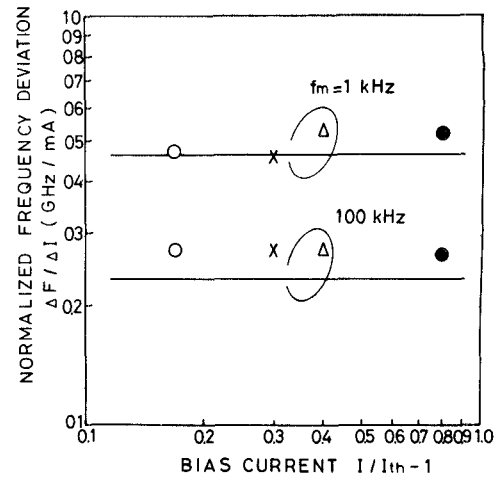

Fig. 18. Bias current dependence of the frequency deviation in the TJS laser low frequency region versus dc drive current. $I_{th,T} = 39$ mA. ○: $1.17 \times I_{th,T}$, ×: $1.3 \times I_{th,T}$, △: $1.4 \times I_{th,T}$, and ●: $1.5 \times I_{th,T}$.

V. STRUCTURE OPTIMIZATION FOR FM LASER APPLICATION

Large frequency deviation with small modulation current, independent from modulation frequency, is desired for an FM laser application. The way to meet this goal is to suppress the gradually decreasing response due to temperature modulation effect and to enhance the flat FM response due to carrier density modulation effect.

To obtain the flat FM response due to carrier density modulation effect, the carrier should be injected to spread outside the effective core region. It is clear from the experimental result shown in Fig. 10 that the BH structure is not suitable for an FM laser. To develop insight on the importance of several parameters in regard to the carrier modulation effect, Fig. 19 shows the normalized frequency deviation in the flat response range between 10 MHz and 1 GHz as a function of the factor-of-two changes in several dimensions about their nominal laser values. The mode confinement factor along vertical direction Γ_y is most important, since frequency deviation is proportional to Γ_y. Small effective core width W_{eff} and refractive index difference Δ_{eff} are efficient in increasing normalized frequency deviation. It should also be pointed out that an increase in dc bias level degrades the normalized frequency deviation.

Several factors which influence the temperature modulation effect are shown in Fig. 20(a) and (b). Static normalized temperature modulation $\Delta T_{eff}/\Delta W$ as a function of the factor-of-two variations in several dimensions is about their nominal laser values for CSP and TJS lasers. Diode length is the most important parameter, since the normalized frequency deviation is inversely proportional to diode length. Stripe width is the next important parameter, which should be increased to suppress the temperature modulation effect. Fig. 21 shows the static normalized temperature modulation versus the factor-of-two variation in stripe width about its nominal value of CSP laser as a function of lasing optical field spot size. The distribution of temperature modulation is shown in Fig. 22 as a function of stripe width. The increase in spot size as well as the increase in A is effective to suppress the temperature modulation effect. The suppression of temperature modulation effect, with increasing L and A, is partially canceled out by the threshold current increase caused by increased L and
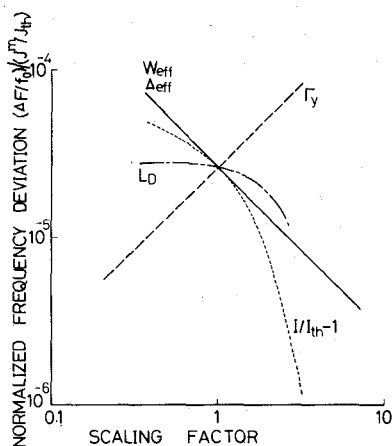
Fig. 19. Normalized frequency deviation in the flat FM response range versus factor-of-two changes in several dimensions about their nominal values. $W_{eff} = 6$ μm, $\Delta_{eff} = 1 \times 10^{-3}$, $I/I_{th} = 1.4$, $\Gamma_x = 0.26$, and $L_D = 3$ μm.
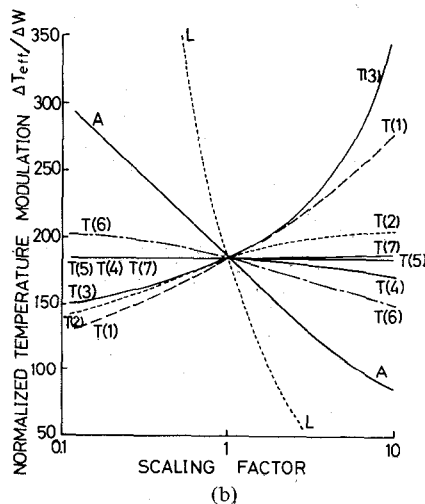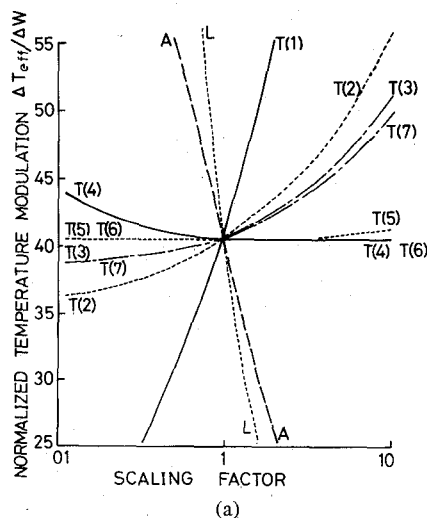

Fig. 21. Normalized effective temperature modulation $\Delta T_{eff}/\Delta W = \int \Delta T_a(x)|\epsilon(x)|^2 \, dx/\Delta W$ (deg/W) at zero modulation frequency versus normalized stripe width A/A_{nom} for CSP laser as a function of lasing optical field spot size.
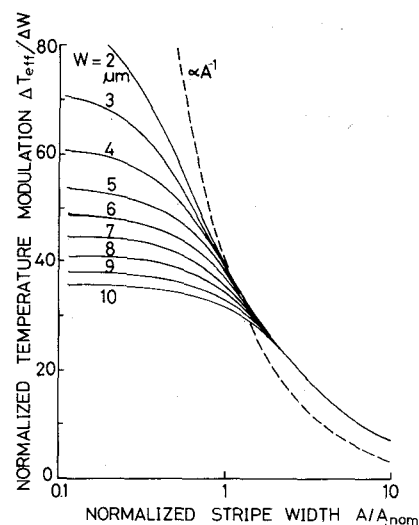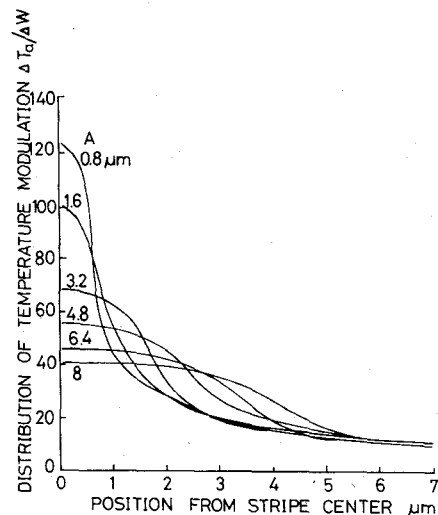

(a)

(b)

Fig. 20. Normalized effective temperature modulation $\Delta T_{eff}/\Delta W = \int \Delta T_a(x)|\epsilon(x)|^2 \, dx/\Delta W$ (deg/W) at zero modulation frequency versus factor-of-two changes in several dimensions about their nominal values. (a) For CSP laser and (b) TJS laser.

Fig. 22. Distribution of normalized temperature modulation $\Delta T_a(x)/\Delta W$ (deg/W) for various stripe width for CSP laser.

A. FM response due to carrier density modulation is also reduced with increasing L and A. Among film thickness values

for each layer, $T(1)$ and $T(3)$ are important and should be minimized to suppress the temperature modulation effect. To eliminate the temperature modulation effect, cutoff modulation frequency should be decreased as well as the static frequency deviation value mentioned above. Fig. 23 shows the step drive current responses in frequency deviation for CSP, BH, and TJS lasers. The p-side up mounted TJS and BH lasers have larger time constants in step pulse response than the p-side down mounted CSP laser by about an order of magnitude. Therefore, TJS and BH lasers have lower cutoff modulation frequencies than the CSP laser. The time constant for a step pulse response is independent of stripe width, and it decreases with decreasing $T(1)$.

Spurious intensity modulation is encountered when direct frequency modulation is performed by the injection current modulation. It should be minimized for an FM laser application. Intensity modulation depth values, accompanied with a 100 MHz frequency deviation for CSP, BH, and TJS lasers,
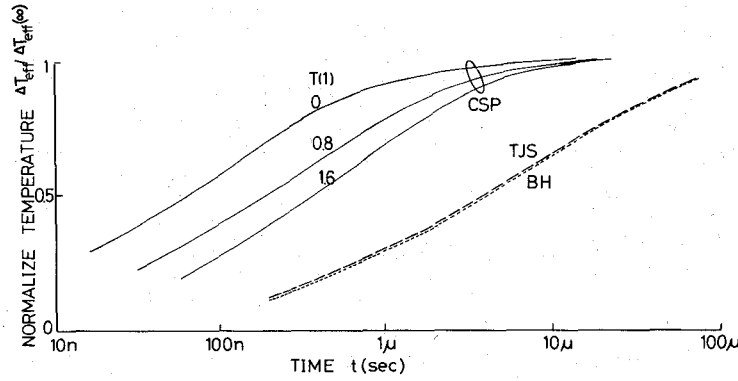
Fig. 23. Step pulse response of effective temperature change for CSP, TJS, and BH lasers.

are summarized in Table I. A several hundred megahertz frequency deviation is obtained with less than 10 percent intensity modulation, which can be easily suppressed if the injection locked semiconductor laser FM signal post-amplifier is employed [21].

VI. CONCLUSION

Direct frequency modulation characteristics in CSP, TJS, and BH AlGaAs lasers are measured in the modulation frequency region between 0 and 5.2 GHz. The experimental results are compared with the theoretical analyses considering carrier modulation effect and temperature modulation effect. Frequency modulation at high modulation frequency stems from the carrier modulation effect, which is satisfactorily described by the rate equation analysis with lateral carrier and optical field profile. Frequency modulation at low modulation frequency, on the other hand, stems from the temperature modulation effect, which is successfully described by the dynamic thermal equation.

The frequency modulation due to carrier modulation effect exhibits a resonance peak due to relaxation oscillation and cutoff characteristics at several gigahertz modulation frequencies. The FM response decreases with increasing dc bias level. Flat FM response is obtained in CSP and TJS lasers, but a V-shaped decrease in FM response at about 100 MHz is observed in the BH laser. The dc bias level and the lateral carrier and optical field confinement configuration dependences of FM response are the most striking and unique characteristics different from direct IM. These characteristics stem from the carrier density modulation which is easily clamped by the lasing optical field.

The frequency modulation characteristics due to temperature modulation effect depend strongly on whether the chip is mounted p-side up or down. A p-side up mounted laser has larger thermal FM response and lower cutoff frequency than a p-side down mounted laser.

Some design considerations for an FM laser application to achieve a flat and efficient FM response with small spurious intensity modulation have been presented. Carrier should also be injected outside the effective core region to cover the evanescent field of a lasing optical mode. Weak lateral mode confinement, strong vertical mode confinement, and a short distance between an active layer and a submount are effective ways to meet the goal.

APPENDIX I
SPURIOUS AMPLITUDE MODULATION

When the phase differences between FM and AM modulations are 0, $\pi/2$, π, and $3\pi/4$, carrier, upper, and lower first-sideband amplitudes are represented as shown in Table II. Fig. 24 shows the relation of the phase difference between FM (carrier density) and AM (photon density) modulation, A, B, C, and D in Fig. 24(a). Various power spectra, corresponding to these phase differences, are represented in Fig. 24(b). Fig. 25 shows the amplitude modulation depth calculated from the power spectra in Fig. 2(a)-(h). Closed circles are calculated from the ratio of modulation current to the bias current minus threshold current. Open circles show the calculated value from the power spectra using the amplitude equations for C in Table II. Good agreement with both calculated values shows that observed experimental results in Fig. 2(a)-(h) show the case of the phase difference of π corresponding to (C) in Fig. 24(a) and (b). It is assumed that the phase differences between photon density and carrier density are also out of phase.

APPENDIX II
COEFFICIENTS $A_{i,j}$ IN EQUATION (28) ARE GIVEN BY

$$A_{11} = j\omega + 1/\tau_p - \alpha\Gamma_y[\bar{N}_{\text{eff}} + \eta(\bar{N}_1 - \bar{N}_2)/2(1 + \eta)]$$

$$A_{12} = -\alpha\Gamma_y\bar{S}_0 - \beta\zeta/\tau_s(1 + \eta)$$

$$A_{13} = -\alpha\Gamma_y\bar{S}_0\,\eta/2(1 + \eta)$$

$$A_{14} = \alpha\Gamma_y\bar{S}_0\,\eta/2(1 + \eta)$$

$$A_{21} = \alpha\Gamma_y[(3/2 + \eta)\,\bar{N}_{\text{eff}} - \bar{N}_1/4 - 3\eta\bar{N}_2/4]$$

$$A_{22} = j\omega + 1/\tau_s + \alpha\Gamma_y\bar{S}_0(3/2 + \eta)$$

$$A_{23} = -(L_D^2/2\tau_s)(2\pi/W_{\text{eff}})^2 - \alpha\Gamma_y\bar{S}_0/4$$

$$A_{24} = -3\alpha\Gamma_y\bar{S}_0\,\eta/4$$

$$A_{31} = -\alpha\Gamma_y[\bar{N}_{\text{eff}} - (1/2 + \eta)\,\bar{N}_1 - \eta\bar{N}_e/2]$$

$$A_{32} = -\alpha\Gamma_y\bar{S}_0$$

$$A_{33} = j\omega + 1/\tau_s + (L_D^2/\tau_s)(2\pi/W_{\text{eff}})^2 + \alpha\Gamma_y\bar{S}_0$$

$$A_{34} = \alpha\Gamma_y\bar{S}_0\,\eta/2$$

$$A_{41} = -\alpha\Gamma_y[\eta\bar{N}_{\text{eff}} - (3/2 + \eta)\,\bar{N}_2]$$

TABLE II
AMPLITUDE OF POWER SPECTRA IN VARIOUS PHASE DIFFERENCES
BETWEEN FM AND AM MODULATION

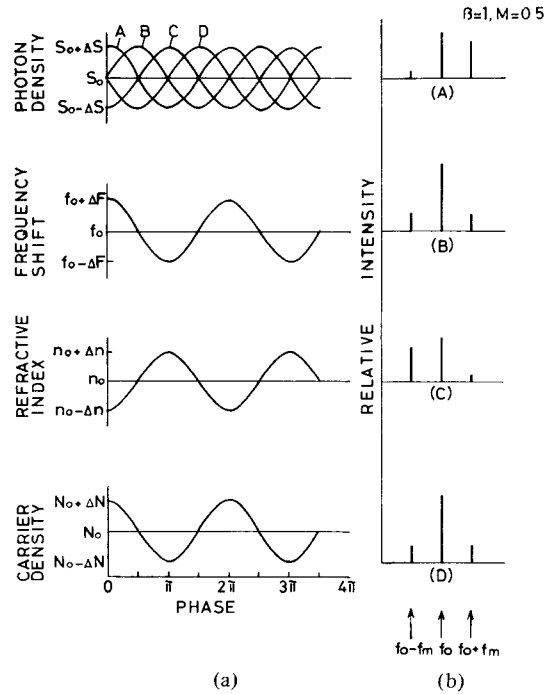|	Phase difference $\Delta\theta$	Carrier f_0	Amplitude Upper Sideband $f_0 + f_m$	Lower Sideband $f_0 - f_m$
A	0	$J_0 E_0$	$E_0\{J_1 + M(J_2 + J_0)/2\}$	$E_0\{-J_1 + M(J_2 + J_0)/2\}$
B	$\pi/2$	$E_0\sqrt{J_0^2 + M^2 J_1^2}$	$E_0\sqrt{J_1^2 + M^2(J_0 - J_2)^2/4}$	$E_0\sqrt{J_1^2 + M^2(J_0 - J_2)^2/4}$
C	π	$J_0 E_0$	$E_0\{J_1 - M(J_0 + J_2)/2\}$	$-E_0\{J_1 + M(J_1 + J_2)/2\}$
D	$3\pi/4$	$E_0\sqrt{J_0^2 + M^2 J_1^2}$	$E_0\sqrt{J_1^2 + M^2(J_0 - J_2)^2/4}$	$E_0\sqrt{J_1^2 + M^2(J_0 - J_2)^2/4}$

(a)   (b)

Fig. 24. Power spectra relations. (a) Relation between photon density, frequency deviation, refractive index, and carrier density. (b) Power spectra at various phase differences between photon density and frequency deviation as shown in Appendix I. Phase differences are A: $\Delta\theta = 0$, B: $\pi/2$, C: π, and D: $3\pi/4$.

$$A_{42} = -\alpha\Gamma_y \bar{S}_0 \eta$$

$$A_{43} = 0$$

$$A_{44} = j\omega + 1/\tau_s + (L_D^2/\tau_s)(\pi/W_{eff})^2 + \alpha\Gamma_y \bar{S}_0(3/2 + \eta).$$

Fig. 25. Amplitude modulation depth obtained by frequency modulated power spectra versus frequency modulation index. o: Obtained from power spectra using the out of phase relation between light amplitude and frequency deviation indicated in Appendix I. •: Obtained from the relation between applied modulation current and threshold current assuming that I-L characteristics are linear.

REFERENCES

[1] Y. Yamamoto, "Receiver performance evaluation of various digital optical modulation–demodulation systems in the 0.5–10 μm wavelength region," *IEEE J. Quantum Electron.*, vol. QE-16, pp. 1251–1260, Nov. 1980.

[2] Y. Yamamoto and T. Kimura, "Coherent optical fiber transmission systems," *IEEE J. Quantum Electron.*, vol. QE-17, pp. 919–935, June 1981.

[3] S. Saito, Y. Yamamoto, and T. Kimura, "Optical heterodyne detection of directly frequency modulated semiconductor laser signal," *Electron. Lett.*, vol. 16, pp. 826–827, Oct. 1980.

[4] ——, "Optical FSK heterodyne detection experiments using semiconductor laser transmitter and local oscillator," *IEEE J. Quantum Electron.*, vol. QE-17, pp. 935–941, June 1981.

[5] M. Nakamura, K. Aiki, N. Chinnone, R. Ito, and J. Umeda, "Longitudinal-mode behaviors of mode-stabilized $Al_xGa_{1-x}As$ injection lasers," *J. Appl. Phys.*, vol. 49, pp. 4644–4648, Sept. 1978.

[6] J. M. Osterwalder and B. J. Rickett, "Frequency modulation of GaAlAs injection lasers at microwave frequency rates," *IEEE J. Quantum Electron.*, vol. QE-16, pp. 250–252, Mar. 1980.

[7] S. Kobayashi, Y. Yamamoto, and T. Kimura, "Modulation frequency characteristics of directly optical frequency modulated AlGaAs semiconductor laser," *Electron. Lett.*, vol. 17, pp. 350–351, May 1981.

[8] K. Aiki, M. Nakamura, T. Kuroda, and J. Umeda, "Channeled-substrate planar structure (AlGa)As injection lasers," *Appl. Phys. Lett.*, vol. 30, no. 12, pp. 649–651, June 1977.

[9] N. Chinone, K. Saito, R. Ito, K. Aiki, and N. Shige, "Highly efficient (GaAl)As buried-heterostructure lasers with buried optical guide," *Appl. Phys. Lett.*, vol. 35, pp. 513–516, Oct. 1979.

[10] H. Namizaki, "Single mode operation of GaAs-GaAlAs TJS-laser diode," *Trans. IECE Japan*, vol. E59, pp. 8–15, May 1976.

[11] T. Kimura and M. Saruwatari, "Temperature compensation of birefringent optical filters," *Proc. IEEE*, vol. 59, pp. 1273–1274, Aug. 1971.

[12] K. Kobayashi and M. Seki, "Microoptic grating multiplexers and optical isolators for fiber-optic communications," *IEEE J. Quantum Electron.*, vol. QE-16, pp. 11–22, Jan. 1980.

[13] M. Ito, T. Ito, and T. Kimura, "Dynamic properties of semiconductor lasers," *J. Appl. Phys.*, vol. 50, pp. 6168–6174, Oct. 1979.

[14] F. R. Nash, "Mode guidance parallel to the junction plane of double-heterostructure GaAs lasers," *J. Appl. Phys.*, vol. 44, pp. 4696–4707, Oct. 1973.

[15] G. H. Thompson, "A theory for filamentation in semiconductor lasers including the dependence of dielectric constant on injected carrier density," *Opto-Electron.*, vol. 4, pp. 257–310, Aug. 1972.
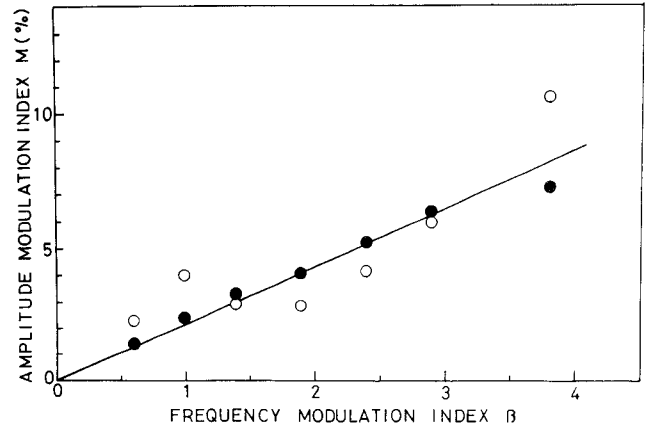
[16] M. Ito and T. Kimura, "Carrier density of refractive index in AlGaAs semiconductor laser," *IEEE J. Quantum Electron.*, vol. QE-16, pp. 910-911, Sept. 1980.

[17] K. Furuya, Y. Suematsu, and T. Hong, "Dependency of spontaneous emission factor on current inhomogeneity of semiconductor laser," *Tech. Group Opt. Quantum Electron.*, paper OQE-77-20.

[18] M. Yano, K. Seki, T. Kamiya, and H. Yanai, "Small signal modulation characteristics of gain-guiding double heterostructure semiconductor lasers," *Trans. IECE Japan*, vol. 61-C, pp. 690-697, Nov. 1978.

[19] M. Ito and T. Kimura, "Stationary and transient thermal properties of semiconductor laser diodes," *IEEE J. Quantum Electron.*, vol. QE-17, pp. 787-795, May 1981.

[20] D. H. Newman, D. J. Bond, and J. Stefani, "Thermal resistance models for proton-isolated double-heterostructure lasers," *Solid State Electron. Dev.*, vol. 2, pp. 41-46, Mar. 1978.

[21] S. Kobayashi, Y. Yamamoto, and T. Kimura, "Optical FM signal amplification and FM noise reduction in an injection locked AlGaAs semiconductor laser," submitted to *Electron. Lett.*

Yoshihisa Yamamoto (S'75–M'80), for a photograph and biography, see this issue p. 421.

Minoru Ito was born in Nagano Prefecture, Japan, on December 4, 1944. He received the B.S. degree in applied physics and the M.S. degree in nuclear engineering from Tokyo Institute of Technology, Tokyo, Japan, in 1967 and 1969, respectively.

After joining the Ibaraki Electrical Communication Laboratory, Nippon Telegraph and Telephone Public Corporation, Ibaraki, Japan, in 1969, he was engaged in the study of optical memory, beam control, and optical fiber property measurement. From 1977 to 1979 he was engaged in research on semiconductor lasers at the Musashino Electrical Communication Laboratory, NTT, Tokyo, Japan. Since 1980, he has been engaged in research on optical devices at Ibaraki Electrical Communication Laboratory.

Mr. Ito is a member of the Institute of Electronics and Communication Engineers of Japan and the Japan Society of Applied Physics.

Soichi Kobayashi (M'80), for a photograph and biography, see this issue, p. 427.

Tatsuya Kimura (S'63–M'68–SM'78), for a photograph and biography, see p. 64 of the January 1982 issue of *IEEE J. Quantum Electron.*

Superhigh Differential Quantum Efficiency and Strong Self-Sustained Pulsation in CW DH Laser Diodes

CHI-MING WANG, LI-QING ZHAO, WAN-RU ZHUANG, JING-MING CHANG, CHUN-SHAN CHANG, AND ZHEN-QIU WU

Abstract—Some experimental results in GaAs DH lasers having a stable, long operating-time, such as nonlinear superhigh differential quantum efficiency, the behavior of light output saturation and sudden growth again in the same filament, strong self-sustained pulsation, and so on, are presented. A model of double filaments caused by the nonuniform distribution of aluminum in the active layer of the laser diode is presented to explain their anomalous behavior qualitatively.

I. INTRODUCTION

THE transient response in laser diodes is an important factor for application to optical communication. At present, the self-sustained pulsations appearing in AlGaAs DH laser diodes interest scientists and engineers. Some mechanisms causing pulsation have been suggested, such as second order mode locking [1], deep-level traps [2], and saturable absorption effect [3]–[5], and so on, but more attention is paid to the latter.

We also have observed this behavior in AlGaAs DH laser diodes made in our laboratory and found some new phenomena. The devices are made by conventional LPE technology on (100) plan of GaAs substrate. Five layers are grown. They are n-GaAs (buffer layer), N-$Al_{0.35}Ga_{0.65}As$ (Te-doped), p-$Al_{0.05}Ga_{0.95}As$ (Si-doped active layer), P-$Al_{0.35}Ga_{0.65}As$ (Ge-doped), and p-GaAs (Ge-doped cap layer). The thickness of the active layer is about 0.3-0.5 μm. Other parameters are the same as those in [6]. The stripe-geometry structure is formed by proton bombardment with a stripe width of 12 μm. The length of the cavity is about 300 μm. The depth on the proton bombardment is just inside the p-type confined layer. Contacts of Cr-Au-Zn and Au-Ge-Ni are applied to the p-side and substrate side of the chips, respectively. The CW threshold current density J_{th} is about 1000-3000 A/cm^2.

II. L-I CHARACTERISTICS ON LASER DIODES

Most laser diodes have a normal L-I curve without "kinks," but some are quite different.

Two kinds of anomalous dc L-I curves have been measured as shown in Fig. 1. Laser diodes A show an anomalous wide flat step, while laser diodes B show an anomalous superhigh